Type of the Paper (Article, Review, Communication, etc.)

Label-Free Imaging of Melanoma with Confocal Photothermal Microscopy: Differentiation between Malignant and Benign Tissue

Takayoshi Kobayashi[1,2,3,4,5,*], Kazuaki Nakata[1,2,3], Ichiro Yajima[6], Masashi Kato[6], Hiromichi Tsurui[7]

[1] Advanced Ultrafast Laser Research Center and Brain Science Inspired Life Support Research Center, University of Electro-Communications, 1-5-1 Chofugaoka, Chofu, Tokyo 182-8585, Japan
[2] JST, CREST, 5 Sanbancho, Chiyoda-ku, Tokyo 102-0075, Japan
[3] Tokyo University of Science, Department of Physics,
[4] Department of Electrophysics, National Chiao-Tung University, 1001 Ta Hsinchu Rd., Hsinchu 300, Taiwan
[5] Research Center for Water Frontier Science and Technology, Tokyo University of Science, Kagurazaka 1-3, Shinjuku-ku, Tokyo, 162-8601, Japan
[6] Department of Occupational and Environmental Health, Graduate School of Medicine, Nagoya University, 65 Tsurumai-cho Showa-ku, Nagoya, Aichi 466-8550, Japan
[7] Department of Pathology, Juntendo University School of Medicine, 2-1-1 Hongo, Bunkyo-ku, Tokyo 113-8421 Japan
*E-mail: kobayashi@ils.uec.ac.jp; Tel.: +81-48-443-5845

Abstract: Label-free confocal photothermal (CPT) microscopy was utilized for the first time to investigate malignancy in mouse skin cells. A laser diode (LD) with 405nm or 488nm was used as a pump and 638nm LD as a probe for the CPT microscope. The Grey Level Cooccurrence Matrix (GLCM) for texture analysis was applied to the CPT images. Nine parameters of GLCM were calculated for the intracellular super-resolved CPT images, and the parameters Entropy and Prominence were found to be most suited among the nine parameters to discriminate between healthy cells and MM cells in case pump wavelength of 488nm is used.

Keywords: photothermal microscopy; label-free imaging; melanoma; texture analysis;

1. Introduction

Malignant melanoma (MM) is one of the most common cancers worldwide. MM has a high chance of cure only if the area affected by MM is removed in the early stage. However, MM reportedly causes a large majority of skin cancer deaths[1]) despite the fact that it accounts for less than 2% of skin cancer cases. The incidence of MM has also been increasing for more than 30 years[2]). One of the most ominous characteristics of MM is its high capability of distant metastasis because it can spread throughout the body through the lymphatic and blood vessels. For this reason, early detection and treatment of MM are crucial life-saving measures[3]). Although dermoscopy is a powerful diagnostic technique[4]) and the ABCDE rule provides a guide to identification of involved areas[5]), pathological examination is still the gold standard for diagnosis of MM. However, diagnosis is still highly reliant on the skill level of the pathologist. Furthermore, interobserver reproducibility of MM diagnosis varies even among experts.

One strategy with which to improve the diagnostic reliability, namely fractal analysis, has been developed. This method is based on calculation of the fractal dimension (FD) of the structure of MM cells and their distribution[6-11]). Although this is a very attractive idea, the method has the following three drawbacks. First, the technique is based on self-similarity; therefore, if no self-similarity is present in the structure, the obtained fractal dimension is difficult to be connect to the structure features being discussed in the paper. Second, the FD is based on calculation of the line length or area of the colored region, and the change in the value is then visualized by changing the domain to be

Peer-reviewed version available at Bioengineering 2018, 5, 67; doi:10.3390/bioengineering5030067

analyzed. This procedure limits the ratio between the minimal size of evaluation and the total size, resulting in limited spatial resolution and spatially dependent information. The last disadvantage is described as follows. As described in the previous paper[12]), marker-free phenotyping of tumor cells by fractal analysis of reflection interference contrast microscopy images results in a very small difference in the value of FD between the two different types of MM cells. The FDs of the two different types of MM cells were 1.353 ± 0.004 and 1.312 ± 0.005 in that report[12]). Hence, the difference was only 0.041, corresponding to only 3.08% of the average value of the two groups. Even though the authors claimed that the standard deviations (SDs) were as small as 0.005 and 0.004, the FDs in Fig. 4 of their paper showed nearly 80% overlap, while the RICM images showed very clear visual differences in the apparent structural features between the two types (Fig. 4a). This means that even when the image patterns are quite different between two images, similar FDs can be obtained, indicating the method is difficult to be applied to diagnosis. This disadvantage forms the basis of our discussion of the diagnostic application of this technique to skin cancer in the present paper.

Melanin carries information about the metabolism and location of melanocytes and melanogenesis; therefore, the distribution of melanin could act as a marker for MM[13, 14]). Two dominant types of melanin (eumelanin and pheomelanin) have a large absorption cross section of visible light without efficient fluorescence emission[15]), resulting in difficulty of imaging of the distribution of MM. However, the nonfluorescent property of melanin enables even more sensitive imaging of MM by employing photothermal (PT) microscopy (PTM), which is the main subject of the present paper.

PTM, which relies on detection of the probe light intensity change by thermal lensing due to local heating of the sample by absorption of the light from a laser, has shown potential in biological imaging and clinical applications. The key advantages of PTM are its high sensitivity and no requirement of staining[16-21]). It allows for imaging of nanometer-sized absorbers buried among scatterers with high resolution and a high signal-to-noise ratio in real time[19, 22, 23]). However, the PT signal intensity in normal PTM has two extrema in the axial direction[24]), which introduces distortions resulting in limited axial resolution of three-dimensional PT images. Confocal PTM (CPTM), which has a detection scheme similar to that of confocal microscopy, can help to remove this drawback and improve the axial resolution[24]). Using CPTM, the authors' group studied super-resolution microscopic images of neurons in mouse brain[25, 26]) and mouse skin MM[27]).

Label-free CPTM with super-resolution was applied to mouse skin cells for the first time to investigate malignancy. A gray-level co-occurrence matrix (GLCM) method was used for texture analysis of the label-free CPTM images of MM to study the differences in intracellular super-resolved structural properties between single MM and nevus cells. Nine parameters of the intracellular moment (ASM) and inverse difference moment (IDM) were found to be the most suited to discriminate between nevus and MM cells. This method is expected to be powerful for diagnosis of MM.

In this study, we developed a CPTM technique for noninvasive label-free imaging of MM from mice for the purpose of future application to humans. RFP/RET-transgenic mice of line 304/B6 (RET-Tg) stepwise develop benign melanocytic tumors and malignant melanomas and widely used for analysis of melanoma genesis[28-30]). The performance of the setup was tested with a sample of 20-nm gold nanoparticles. Using the PT imaging data, we then analyzed the structural properties of MM and nevus cells to be compared using the GLCM method[31-37]). We calculated nine different parameters: ASM, contrast, correlation, entropy, IDM, homogeneity, prominence, shade, and variance. These textural parameters were calculated by analyzing relevant regions of interest on 12 two-dimensional PT images taken at two different positions in three tissue sections containing nevus and MM cells. The details of analysis are described in the following Experimental section. Our method provides an objective evaluation which is not dependent on the experience, skill, and knowledge of individual medical doctors, and prognostication at each occasion of the pathology diagnosis. Thus GLCM calculation provides a quantitative indicator, which may become a "standard" in future by accumulating the clinical cases in real medical sites composed of various

people with variety of experiences. We defined a new index DISC for the discrimination between nevus and MM cells. We found that the Entropy and Homogeneity in the case of 405 nm pump, and Entropy and Prominence in the case of 488 nm pump were the two most suited among the nine parameters for discrimination between nevus and MM cells in a mouse. This research received no external funding

2. Materials and Methods

2.1. Mice

Nevus and MM samples in transgenic mice (RET-Tg) carrying constitutively activated c-RET28-30) were prepared, and then 16-μm-thick paraffin sections were used for analysis. The Animal Care and Use Committee (approval no. 270108 in Juntendo University) and the recombination DNA Advisory Committee (approval no. 13–7626-55 in Juntendo University approved this study.

2.2. Experimental Setup and Image-Taking Procedure

A 405-nm laser diode (LD) (NDV4316; Nichia, Tokushima, Japan) and a 488-nm LD (L488P60; Thorlabs, Newton, NJ, USA) were used for the pump laser. A 638-nm LD (ML520G55; Mitsubishi, Tokyo, Japan) was used for the probe. The pump laser was modulated at 100 kHz using signal generators, and the two LDs were introduced to beam collimators. After combination of the pump and probe beams using a dichroic mirror, the probe was split by a polarized beam splitter for balance detection and then directed to a galvano mirror (VM500PLUS; GSI Group, Bedford, MA, USA). A 4F optical system was located near the sample and objective lens (MPLFNF 40× with numerical aperture of 0.75; Olympus, Tokyo, Japan). Two-dimensional images of the samples were obtained by scanning laser beams with the galvano mirror in the X–Y plane. The irradiation powers of the pump and probe lasers were 300 μW (405 nm), 1.5 mW (488 nm), and 3 mW, respectively. An auto-balanced detector (New Focus Nirvana; Newport Inc., Irvine, CA, USA) composed of two sets of a photodiode and a lock-in amplifier (7270 Signal Recovery; Ametek, Berwyn, PA, USA) was used to remove the probe noise. The frame size of the image was 600 × 600 pixels, which corresponds to a 72- × 72-μm area. The lock-in amplifier sensitivity was 1 mV, and the time constant was 20 μs per point. For the GLCM analysis, a four-section tiled area (18 × 18 μm out of 36 × 36 μm) in the X–Y plane was imaged for each 72 × 72 μm image. We have analyzed 48 images of 18 × 18 μm area in total for both nevus and MM samples.

3. Results

The images of cell samples of about 1 ◎m on 1 mm-thick microscope substrate plates are shown in Figs. 1, 2 and 3. Fig. 1 shows a photograph of cutaneous tissues taken from mice with MM. Microscopic regions of 72 × 72 μm^2 in the PT images were selected out of the image areas for analysis as shown in Figs. 2 and 3. Two bright field images in Fig. 2 are taken with CCD (DCC1645C, Thorlabs) for the nevus sample (top left) and the malignant melanoma (bottom left) with Obj. lens x40. The wavelength and power of excitation LD was 0.3 mW and 405-nm, respectively. Top and bottom right are the PT images with 405-nm pump (600 × 600 pixels, 120 nm / pixel) of nevus and malignant melanoma, respectively. Red squares in bright field images show areas of PT images in 72 × 72 μm^2. Four equal size (18 μm × 18 μm) areas segmented from the red square (36 μm × 36 μm) area in the PT images are used for GLCM analysis. In Fig. 3, top left and top right are the bright field CCD images of nevus sample and malignant melanoma, respectively, with Obj. lens x40 for 488-nm excitation in the same condition as the one in Fig. 2. The top and bottom right images are the PT images with 488-nm pump (600 × 600 pixels, 120 nm / pixel) of nevus and malignant melanoma, respectively. Red squares in the bright field images show areas of PT images in 72 × 72 μm^2. Four equal size (18 μm × 18 μm) areas were segmented out of the four green square areas in the PT images are used for GLCM analysis. The PT images were measured for 12 areas and the 48 calculation regions were selected for both 405- and 488-nm excitation.

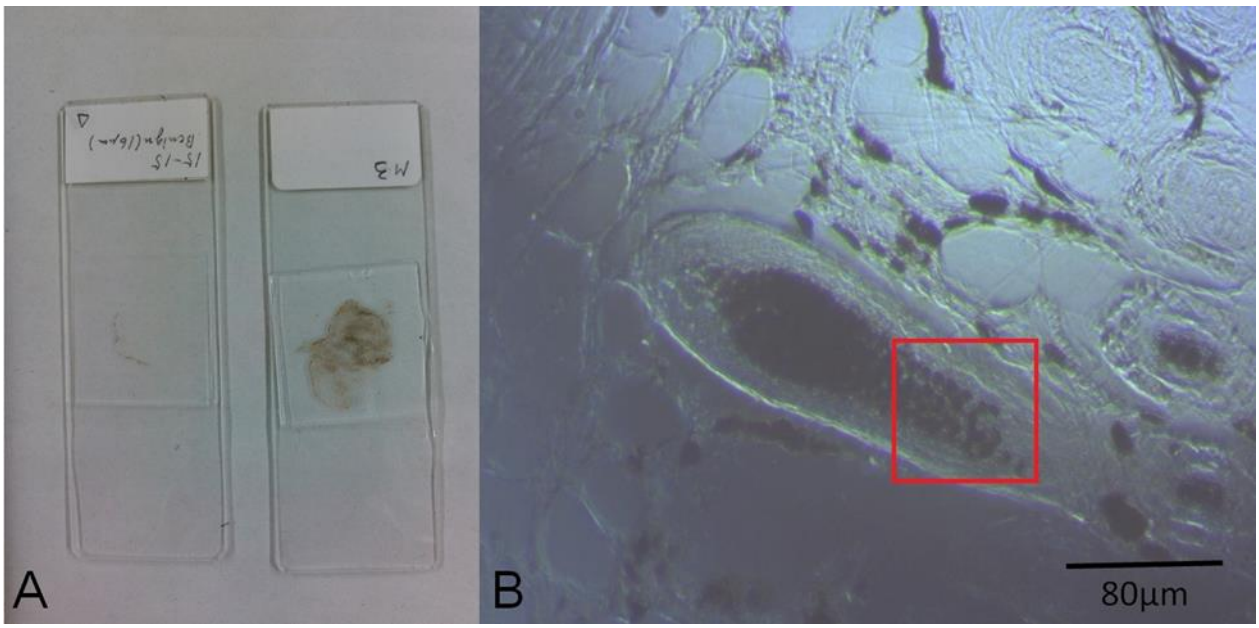

Figure 1. (A) Photo of the prepared specimens. (B) CCD image of a nevus (Obj. lens x10).

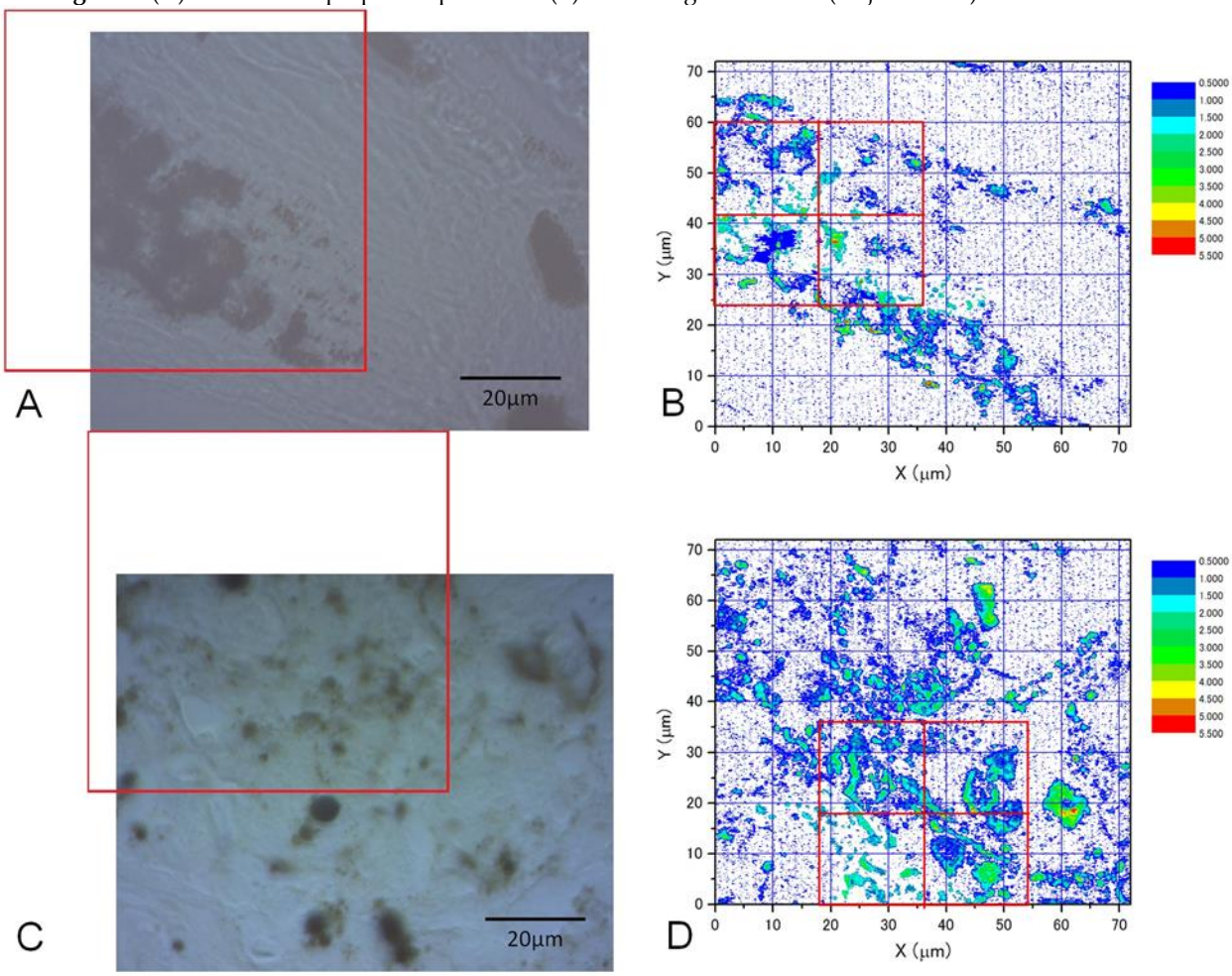

Figure 2. (A) Top left: CCD image and PT image of nevus sample (Obj. lens x40); (C): malignant melanoma (Obj. lens x40) with 405-nm pump. (B) and (D) right show four equal size (18 μm × 18 μm) areas segmented from the red square (36 μm × 36 μm) area are used for GLCM analysis.

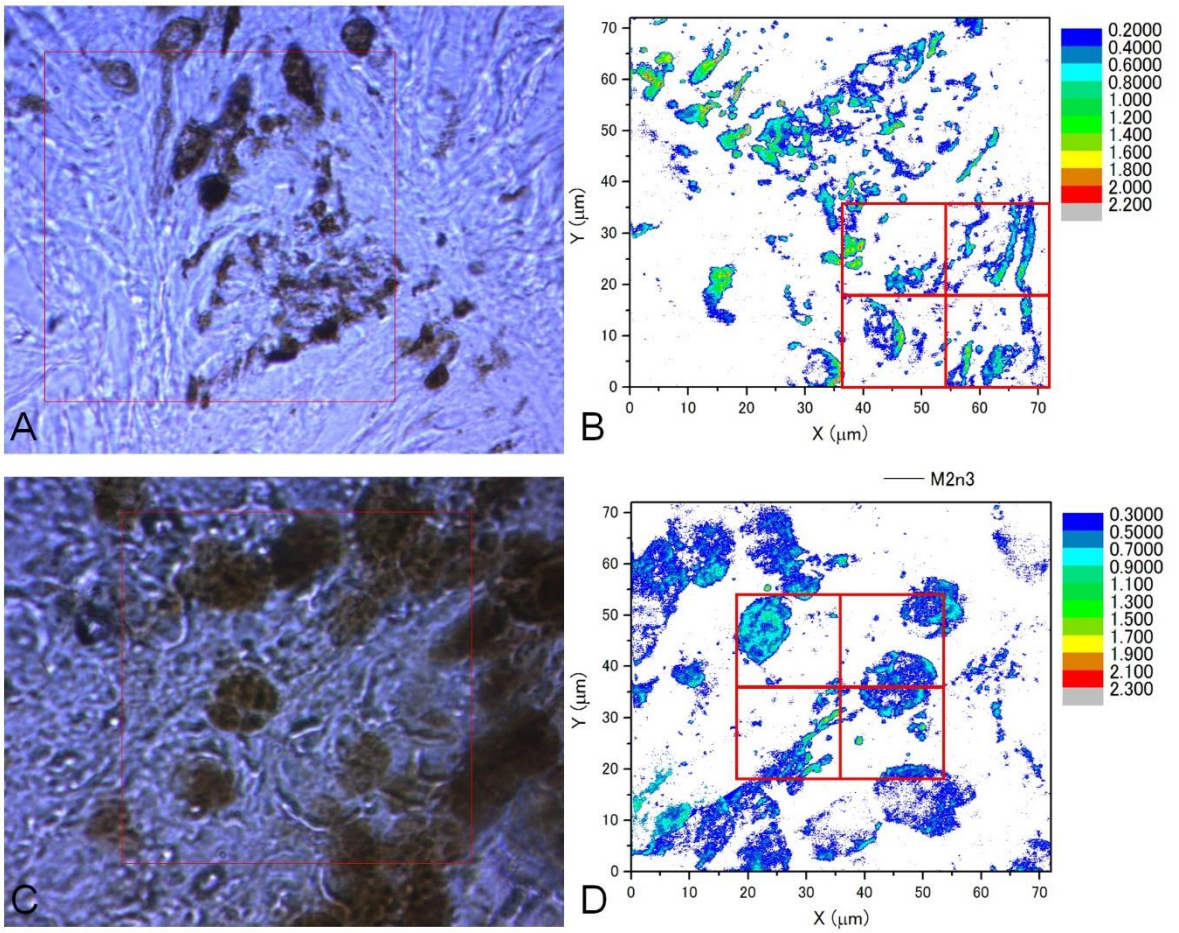

Figure 3. (A): CCD image and PT image of nevus sample (Obj. lens x40); (C): malignant melanoma (Obj. lens x40) with 488-nm pump. (B) and (D) four equal size (18 μm × 18 μm) areas segmented from the four green square areas in the PT images are used for GLCM analysis.

4. Discussion

The textural structure of the images of the mouse skin samples containing both nevus and MM cells taken with the PT imaging method were analyzed by GLCM. The nine parameters were calculated as shown below. The areas of imaging data within the green lines in Fig. 2 at 405 nm excitation were analyzed by the GLCM method, and the 8-bit level gray level intensity distribution of the PT signal is shown in Fig. 4. 12 images of 72 × 72 um to multiple samples of excitation at 488 nm for both nevus and MM samples were also obtained. The areas of imaging data within the green lines in Fig. 3 (left) at 488 nm excitation were analyzed by the method, and the 8-bit level gray level intensity distribution of the PT signal is shown in Fig. 5. Four sets of 18 × 18 um areas (show Figs. 2 and 3) which show higher intensity out of 12 images were chosen and analyzed by the GLMC analysis. There are altogether 48 images of 18 × 18 μm area for both nevus and MM. With these enough number of data groups and data obtained with two pump wavelengths, our statistical reliability is further enhanced. As can be seen from the bright images the sample areas are selected out of various parts of skin. For the method to become a standard method much more samples from larger number of various patients, but as discussed below we discovered two out of nine GLMC parameters are clearly showing the discrimination between nevus and MM, and hopefully used as a criterion for the pathology diagnosis.

Preprints (www.preprints.org) | NOT PEER-REVIEWED | Posted: 19 June 2018 doi:10.20944/preprints201806.0303.v1

Peer-reviewed version available at Bioengineering 2018, 5, 67; doi:10.3390/bioengineering5030067

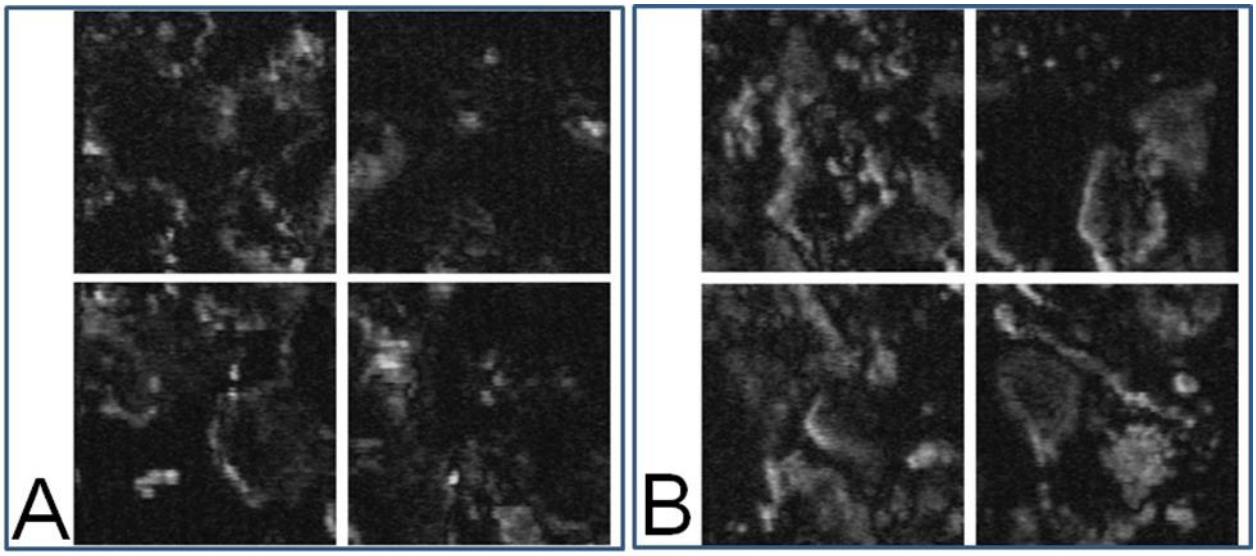

Figure 4. (A): Eight-bit gray level PT image of nevus sample (Obj. lens x40), the four images are corresponding to four segmented areas by the four red squares on the top of PT images in Figure 2; (B): malignant melanoma sample (Obj. lens x40). The four images are corresponding to segmented areas by the four red squares on the bottom of PT images in Figure 2.

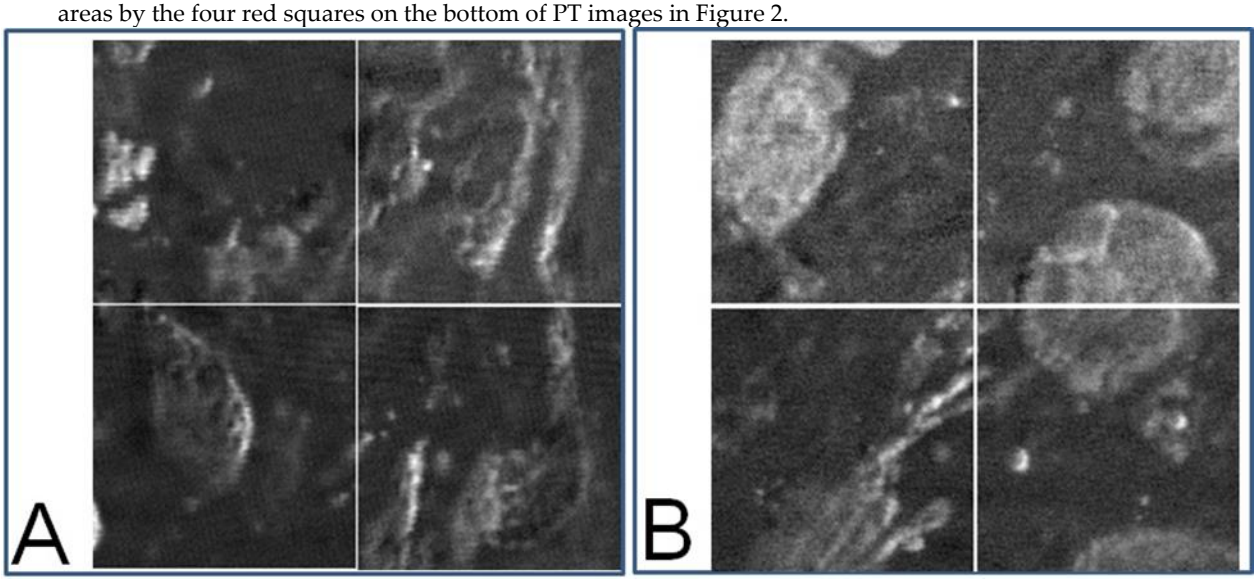

Figure 5. (A): Eight-bit gray level PT image of nevus sample (Obj. lens x40), the four images are corresponding to four segmented areas by the four red squares on the top of PT images in Figure 3; (B): malignant melanoma sample (Obj. lens x40). The four images are corresponding to segmented areas by the four red squares on the bottom of PT images in Figure. 3.

Hereafter the formalism of GLCM is described[38, 39] by showing nine parameters out of most frequently used indexes.

In all of the following formulas, P(i;j) stands for the (i;j)th entry or value in a normalized GLCM.

$$ASM = \sum_{i=0}^{G-1}\sum_{j=0}^{G-1}\{P(i,j)\}^2 \quad (1)$$

$$Contrast = \sum_{|i-j|=0}^{G-1} |i-j|^2 \{\sum_{i=1}^{G}\sum_{j=1}^{G} P(i,j)\} \quad (2)$$

$$Correlation = \sum_{i=0}^{G-1}\sum_{j=0}^{G-1}[\frac{\{i\times j\}\times P(i,j) - \{\mu_x \times \mu_y\}}{\sigma_x \times \sigma_y}] \quad (3)$$

$$Entropy = -\sum_{i=0}^{G-1}\sum_{j=0}^{G-1} P(i,j)\times \log(P(i,j)) \quad (4)$$

$$Homogeneity = \sum_{i=0}^{G-1}\sum_{j=0}^{G-1}\frac{1}{1+|i-j|}P(i,j) \quad (5)$$

$$IDM = \sum_{i=0}^{G-1}\sum_{j=0}^{G-1}\frac{1}{1+(i-j)^2}P(i,j) \quad (6)$$

$$Prominence = \sum_{i=0}^{G-1}\sum_{j=0}^{G-1}(i+j-\mu_x-\mu_y)^4 P(i,j) \quad (7)$$

$$Cluster\ Shade = \sum_{i=0}^{G-1}\sum_{j=0}^{G-1}(i+j-\mu_x-\mu_y)^3 P(i,j) \quad (8)$$

$$Variance = \sum_{i=0}^{G-1}\sum_{j=0}^{G-1}(i-\mu)^2 P(i,j) \quad (9)$$

$$\mu_x = \sum_{i=0}^{G-1} i \sum_{j=0}^{G-1} P(i,j) \quad (10)$$

$$\mu_y = \sum_{j=0}^{G-1} j \sum_{i=0}^{G-1} P(i,j) \quad (11)$$

$\mu_x = \mu_y = \mu$ for a symmetric matrix.

Tables I-IV show the nine parameters calculated from distance parameters d=1-10 (equivalent to 240-2400 nm, respectively) for nevus and malignant melanoma samples, respectively.

Figs. 6 and 7 depict the bar chart of the nine calculated parameters being averaged for distance parameters d=1-10 and their standard deviations (SDs). In the Tables and the graph, the bar and value after +- are the dispersion of corresponding parameter values for the four sets of the image data shown in Figs. 4 and 5.

Table I. Calculated GLMC parameters and their standard deviations (SDs) for nevus cells PT image with 405-nm pump.

d	ASM ($\times 10^{-4}$)	Contrast	Correlation ($\times 10^{-4}$)	Entropy	Homogeneity($\times 10^{-1}$)	IDM ($\times 10^{-1}$)	Prominence ($\times 10^{8}$)	Shade ($\times 10^{5}$)	Variance
1	6.83±1.42	140±40	12.7±4.7	7.74±0.23	2.03±0.14	1.18±0.12	1.23±0.50	4.44±1.56	778±224
2	5.37±1.18	370±110	10.6±3.8	7.98±0.24	1.55±0.12	0.82±0.08	1.07±0.45	4.01±1.42	779±224
3	5.05±1.17	560±180	9.0±3.6	8.05±0.26	1.44±0.12	0.74±0.08	0.90±0.40	3.52±1.28	779±225
4	4.89±1.18	710±250	7.8±3.5	8.09±0.26	1.39±0.13	0.70±0.09	0.76±0.37	3.10±1.18	780±230
5	4.76±1.21	830±300	6.8±3.4	8.12±0.27	1.36±0.14	0.69±0.09	0.66±0.35	2.78±1.12	779±237
6	4.65±1.22	930±340	6.0±3.2	8.14±0.28	1.33±0.14	0.67±0.09	0.59±0.33	2.53±1.08	780±243
7	4.57±1.21	1010±380	5.3±3.1	8.15±0.28	1.31±0.14	0.66±0.09	0.53±0.30	2.35±1.04	781±249
8	4.53±1.24	1070±400	4.8±3.0	8.16±0.28	1.29±0.12	0.65±0.07	0.48±0.28	2.19±1.00	781±254
9	4.45±1.24	1130±430	4.4±2.9	8.16±0.28	1.28±0.13	0.64±0.08	0.44±0.26	2.05±0.96	781±257
10	4.42±1.25	1170±440	4.0±2.8	8.17±0.28	1.27±0.14	0.63±0.09	0.40±0.24	1.92±0.90	779±258

Table II. Calculated GLMC parameters and their standard deviations (SDs) for nevus cells PT image with 488-nm pump.

Peer-reviewed version available at Bioengineering 2018, 5, 67; doi:10.3390/bioengineering5030067

d	ASM ($\times10^{-4}$)	Contrast	Correlation ($\times10^{-3}$)	Entropy	Homogeneity ($\times10^{-1}$)	IDM ($\times10^{-2}$)	Prominence ($\times10^{7}$)	Shade ($\times10^{5}$)	Variance
1	5.72±4.23	547±595	1.44±1.15	8.09±0.68	1.49±0.52	7.81±3.63	2.66±2.07	1.05±1.04	515±238
2	5.66±4.17	538±501	1.39±1.03	8.10±0.67	1.48±0.48	7.81±3.42	2.34±1.77	0.94±0.95	516±239
3	5.41±3.94	616±495	1.16±0.87	8.14±0.65	1.39±0.42	7.09±2.93	1.93±1.47	0.81±0.84	516±239
4	5.42±3.94	605±420	1.12±0.74	8.14±0.64	1.42±0.41	7.31±2.90	1.67±1.22	0.70±0.74	516±240
5	5.26±3.85	729±480	0.84±0.66	8.18±0.63	1.33±0.40	6.74±2.74	1.37±1.07	0.61±0.66	516±241
6	5.23±3.84	758±480	0.76±0.61	8.18±0.63	1.34±0.40	6.79±2.78	1.23±0.95	0.55±0.60	517±242
7	5.12±3.74	806±501	0.64±0.51	8.20±0.62	1.29±0.38	6.45±2.55	1.11±0.86	0.50±0.56	517±243
8	5.15±3.79	770±419	0.67±0.50	8.19±0.62	1.33±0.39	6.71±2.72	1.10±0.81	0.47±0.52	517±243
9	5.06±3.70	865±514	0.51±0.53	8.20±0.61	1.29±0.39	6.45±2.70	0.98±0.76	0.44±0.49	517±244
10	5.04±3.70	856±469	0.49±0.47	8.21±0.61	1.28±0.38	6.41±2.58	0.96±0.71	0.42±0.47	516±246

Table III. Calculated GLCM parameters and their standard deviations (SDs) for malignant melanoma cells PT image with 405-nm pump.

d	ASM ($\times10^{-4}$)	Contrast	Correlation ($\times10^{-4}$)	Entropy	Homogeneity ($\times10^{-1}$)	IDM ($\times10^{-1}$)	Prominence ($\times10^{8}$)	Shade ($\times10^{5}$)	Variance
1	4.88±1.64	160±30	8.29±1.45	8.09±0.25	1.93±0.15	1.10±0.12	1.31±0.17	5.17±0.65	1150±180
2	3.60±1.14	510±70	6.79±0.71	8.40±0.22	1.41±0.09	0.72±0.07	1.08±0.22	4.52±0.80	1150±170
3	3.38±1.26	750±170	6.01±1.19	8.48±0.26	1.30±0.15	0.65±0.10	0.92±0.14	4.01±0.58	1150±180
4	3.18±1.22	1000±230	5.03±1.11	8.54±0.27	1.22±0.16	0.60±0.11	0.74±0.14	3.42±0.57	1150±180
5	3.03±1.18	1240±290	4.15±1.06	8.58±0.27	1.16±0.16	0.56±0.11	0.61±0.14	2.92±0.58	1150±170
6	2.91±1.16	1430±330	3.42±0.99	8.61±0.27	1.13±0.16	0.54±0.11	0.52±0.14	2.54±0.59	1160±170
7	2.82±1.13	1590±350	2.82±0.92	8.63±0.27	1.10±0.16	0.53±0.11	0.45±0.14	2.25±0.58	1160±170
8	2.74±1.11	1730±370	2.32±0.84	8.65±0.26	1.06±0.16	0.50±0.10	0.40±0.13	2.03±0.56	1160±170
9	2.66±1.09	1850±380	1.89±0.77	8.67±0.26	1.03±0.15	0.47±0.10	0.36±0.12	1.85±0.53	1170±170
10	2.60±1.09	1950±400	1.55±0.74	8.68±0.26	1.03±0.18	0.49±0.12	0.33±0.11	1.72±0.49	1170±170

Table IV. Calculated GLCM parameters and their standard deviations (SDs) for malignant melanoma cells PT image with 488-nm pump.

Preprints (www.preprints.org) | NOT PEER-REVIEWED | Posted: 19 June 2018 doi:10.20944/preprints201806.0303.v1

Peer-reviewed version available at Bioengineering 2018, 5, 67; doi:10.3390/bioengineering5030067

d	ASM ($\times10^{-4}$)	Contrast	Correlation ($\times10^{-3}$)	Entropy	Homogeneity ($\times10^{-1}$)	IDM ($\times10^{-2}$)	Prominence ($\times10^{7}$)	Shade ($\times10^{5}$)	Variance
1	4.43±3.54	310±191	1.09±0.52	8.32±0.57	1.56±0.37	8.22±2.70	6.61±3.68	2.44±1.60	931±418
2	4.27±3.45	378±176	1.01±0.45	8.36±0.55	1.50±0.33	7.83±2.41	6.06±3.49	2.25±1.52	932±417
3	4.04±3.31	493±179	0.90±0.36	8.42±0.54	1.40±0.30	7.13±2.17	5.38±3.28	2.03±1.43	932±417
4	3.95±3.28	583±189	0.80±0.28	8.45±0.54	1.38±0.30	7.00±2.23	4.85±3.17	1.83±1.36	933±416
5	3.78±3.16	691±208	0.71±0.23	8.50±0.54	1.31±0.28	6.51±2.07	4.39±3.02	1.67±1.29	934±416
6	3.68±3.08	780±238	0.63±0.19	8.52±0.53	1.27±0.27	6.25±1.96	4.07±2.94	1.55±1.24	935±415
7	3.58±3.03	885±274	0.54±0.17	8.54±0.53	1.20±0.26	5.82±1.83	3.78±2.81	1.46±1.20	936±415
8	3.58±3.02	884±275	0.54±0.18	8.54±0.53	1.24±0.28	6.12±2.06	3.73±2.79	1.40±1.16	936±415
9	3.49±2.96	966±303	0.48±0.17	8.56±0.53	1.18±0.26	5.71±1.84	3.52±2.67	1.34±1.13	936±415
10	3.47±2.93	1000±320	0.45±0.18	8.56±0.52	1.18±0.27	5.70±1.92	3.42±2.63	1.29±1.09	936±415

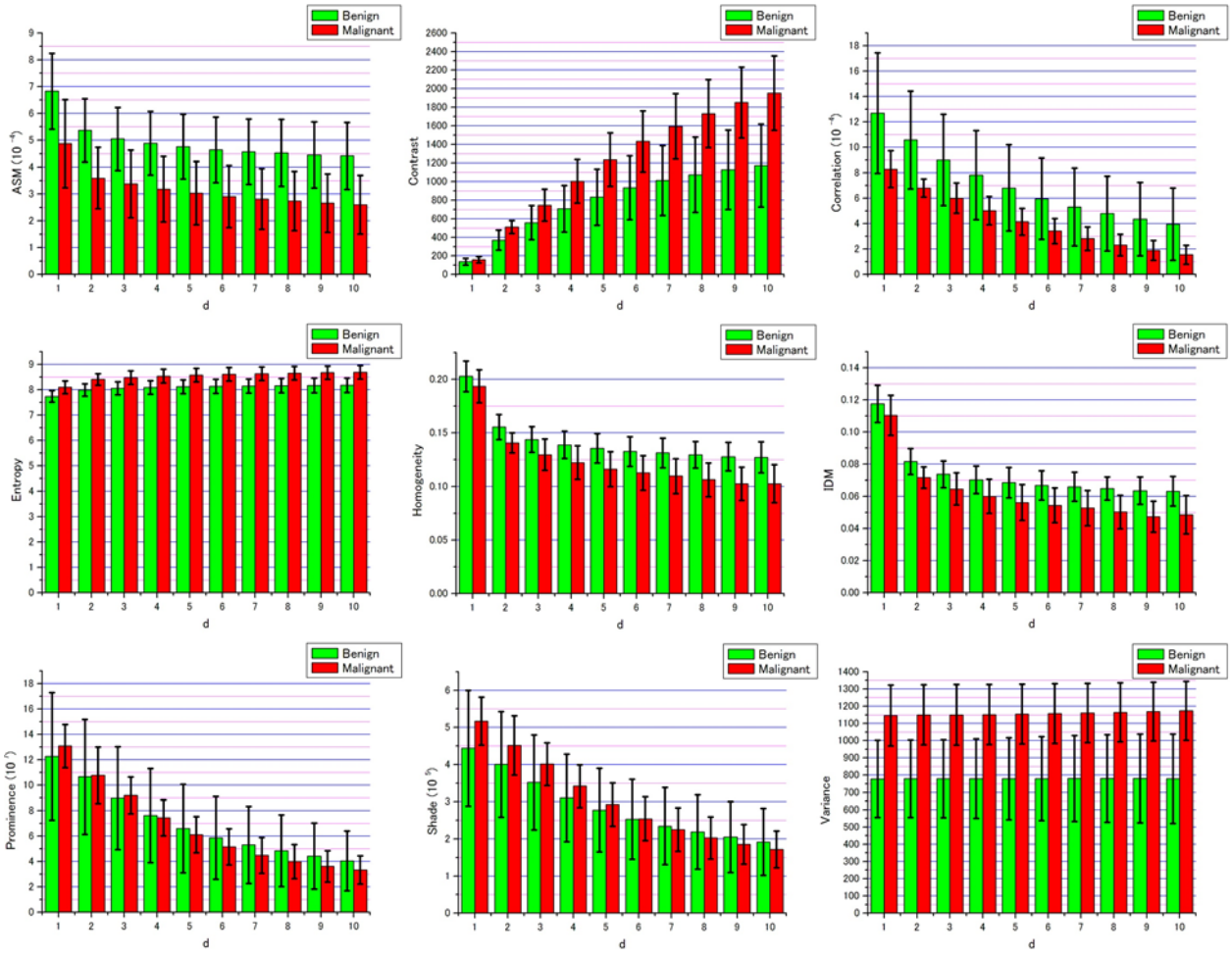

Figure 6. Histograms of nine calculated GLMC parameters (ASM, Contrast, Correlation, Entropy, Homogeneity, IDM, Prominence, hade, Variance) nevus (green), and malignant melanoma (MM) sample (red).

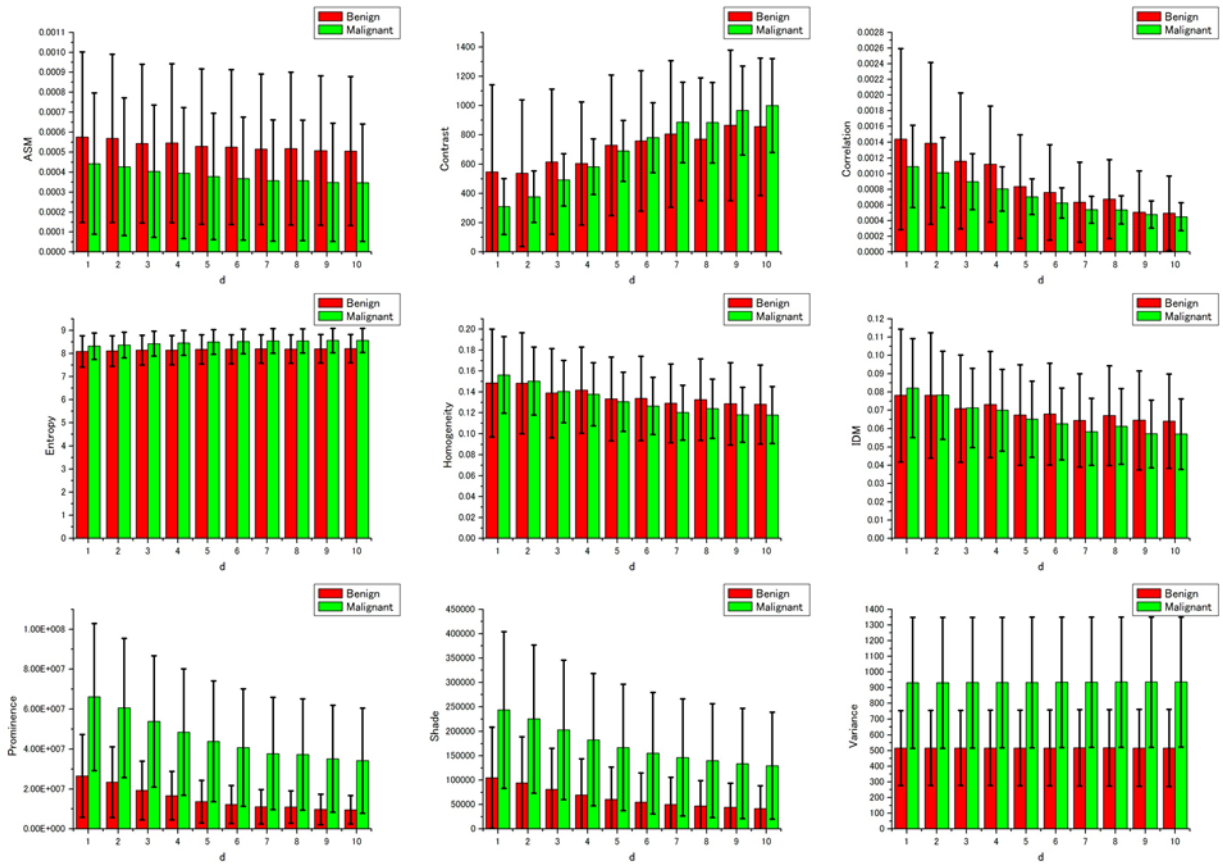

Figure 7. (B) Histograms of nine calculated GLMC parameters (ASM, Contrast, Correlation, Entropy, Homogeneity, IDM, Prominence, hade, Variance) nevus (red), and malignant melanoma (MM) sample (green).

The features shown in Figs. 6 and 7 and Tables I-IV are summarized as follows.

The GLCM analysis of the PT images with 405-nm excitation showed that among the nine parameters, the ASM, entropy, homogeneity, and IDM had well separated values between the nevus and MM cells beyond the sum of the corresponding SD of the two cell species for all values of distance parameter d. The difference in contrast and variance between the two cell types (MM and nevus) was smaller than the sum of the SD values but larger than the larger SD for all values of distance parameter d. The difference in correlation and prominence between the two cell types (MM and nevus) was smaller than the larger SD for all values of distance parameter d. The difference in shade for short distances ($d < 4$) between the two cell types (MM and nevus) was smaller than the SD.

GLCM analysis of the PT images obtained by 488-nm excitation was also performed. Among the nine parameters, entropy, prominence, shade, and variance were well separated between the nevus and MM cells compared with the other parameters. In these cases, the difference between the two cell types (MM and nevus) was smaller than the sum of the SD values but larger than the larger SD for all values of distance parameter d. The difference in the other parameters between the two cell types (MM and nevus) was smaller than the larger SD for all values of distance parameter d. To obtain suitable parameters for the identification of MM, we analyzed the data with a commonly used diagnostic method including the parameters sensitivity, specificity, positive predictive value, and negative predictive value. For the diagnosis, we obtained the fitted Gaussian curves corresponding to the data for $d = 10$ in Tables I-IV for each GLMC parameter; these data are shown in Figs. 8 and 9. We call this the GLMC-DIAG method. The results are listed in Tables V and VI using the data shown in Figs. 8 and 9.

Preprints (www.preprints.org) | NOT PEER-REVIEWED | Posted: 19 June 2018 doi:10.20944/preprints201806.0303.v1

Peer-reviewed version available at Bioengineering 2018, 5, 67; doi:10.3390/bioengineering5030067

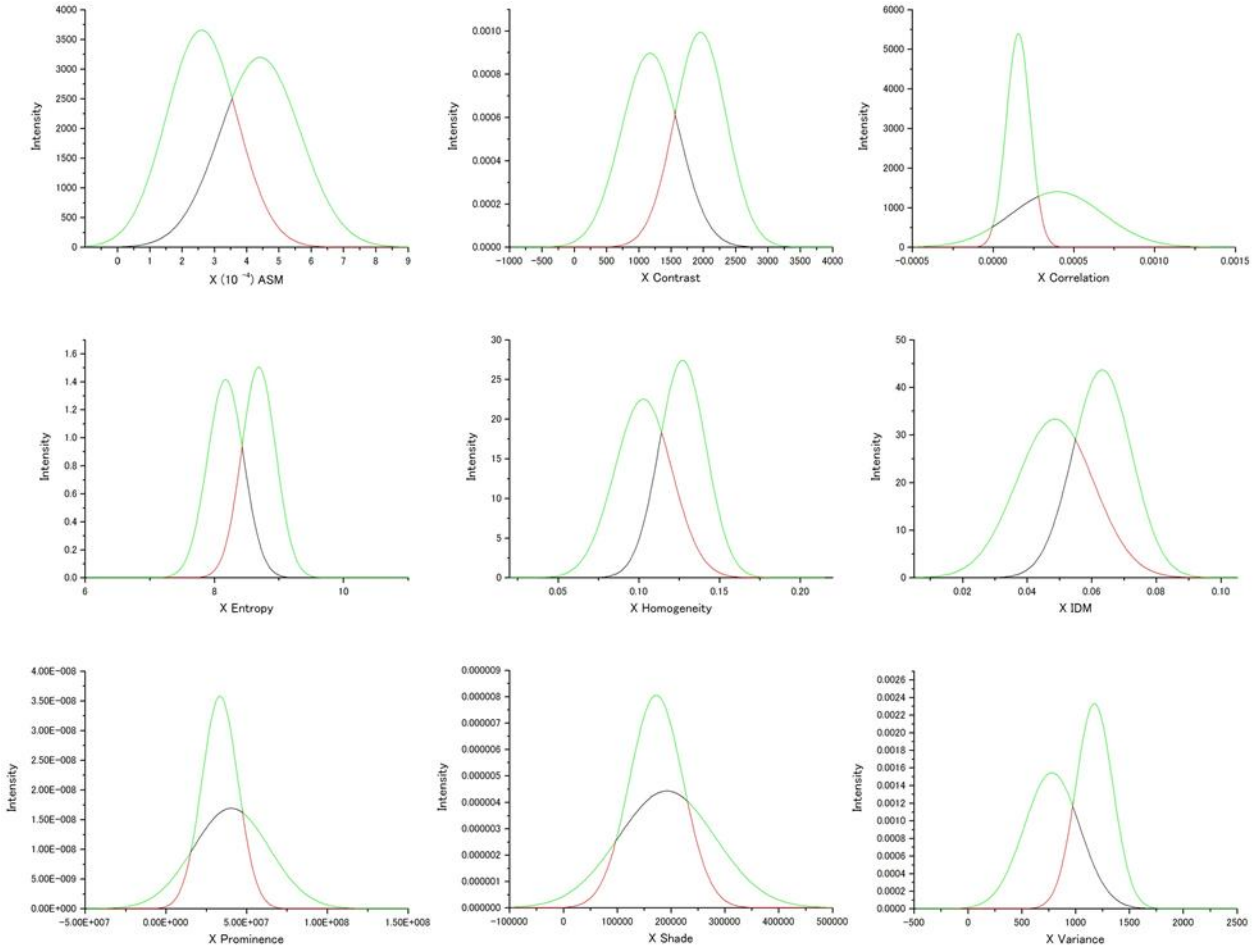

Figurer 8. Gaussian distribution of the parameters fitted to the observed values of the parameters in 405-nm excitation.

Preprints (www.preprints.org) | NOT PEER-REVIEWED | Posted: 19 June 2018 doi:10.20944/preprints201806.0303.v1

Peer-reviewed version available at Bioengineering 2018, 5, 67; doi:10.3390/bioengineering5030067

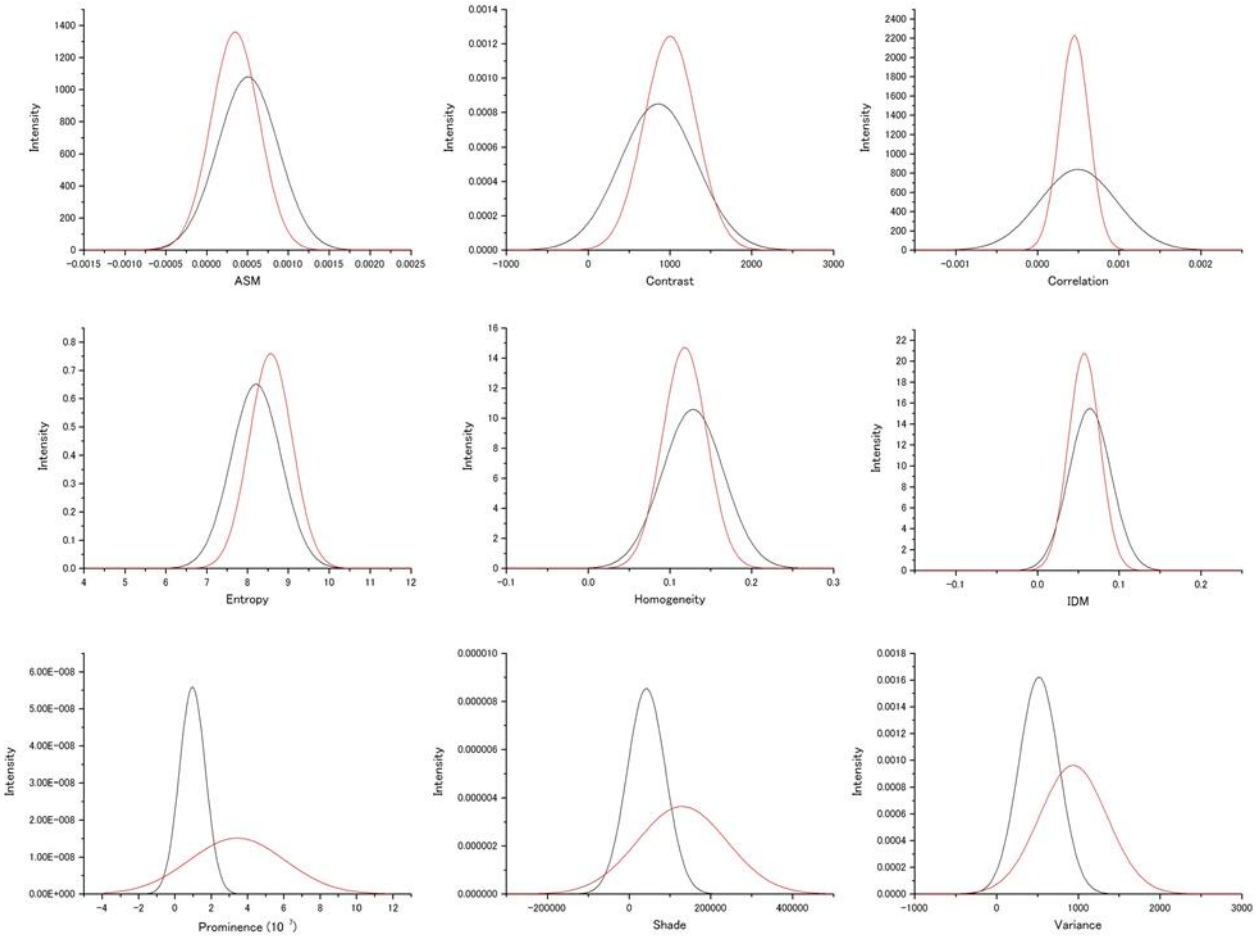

Figure 9. Gaussian distribution of the parameters fitted to the observed values of the parameters in 488-nm excitation.

Table V. Results of calculated GLMC diagnosis method (405-nm excitation).

Parameter	SN	SP	AC	LR+	LR-	PPV	NPV
ASM	0.8017	0.7630	0.7823	3.382	0.2600	0.7717	0.7938
IDM	0.6972	0.8224	0.7599	3.927	0.3681	0.7970	0.7310
Contrast	0.8350	0.8100	0.8225	4.394	0.2038	0.8146	Accuracy

Table VI. Results of calculated GLMC diagnosis method (488-nm excitation).

Parameter	SN	SP	AC	LR+	LR-	PPV	NPV
ASM	0.722	0.461	0.592	1.34	0.603	0.573	0.624
Contrast	0.826	0.370	0.598	1.31	0.471	0.567	0.680
Correlation	--	--	--	--	--	--	--
Entropy	0.706	0.547	0.627	1.56	0.537	0.609	0.651
Homogeneity	0.813	0.356	0.585	1.26	0.526	0.558	0.656

IDM	0.811	0.350	0.580	1.25	0.540	0.555	0.649
Prominence	0.683	0.954	0.819	14.8	0.332	0.937	0.751
Shade	0.592	0.908	0.750	6.42	0.450	0.865	0.690
Variance	0.647	0.858	0.753	4.57	0.411	0.820	0.709

As shown in Table V, variance, entropy, and contrast had large accuracy (AC) and positive likelihood (LR+) values and a small negative likelihood (LR-) value, indicating that these three GLMC parameters are more reliable than the other GLMC parameters.

As shown in Table VI, prominence, shade, and variance had large AC and LR+ values and a small LR- value, indicating that these three GLMC parameters are more reliable than the other GLMC parameters.

Next, we developed an even simpler analysis than the GLMC-DISC method.

The values calculated for the nine GLCM parameters are listed in Tables I-IV.

To obtain suitable parameters for the identification of MM, we defined the difference criterion (DIF) as follows:

$$DIF = |(PM - PB)| / [(\mathrm{DM} + \mathrm{DB}) / 2] \quad (12)$$

Here, PM and PB are the parameter values of the MM and nevus cells, respectively, and DM and DB are the SDs of PM and PB for the four sets of imaging data. The orders of the sizes and values of the DIF for the nine parameters are shown in Tables VII-X, respectively. Entropy and variance were still ranked in the top 1 and 2 positions, respectively, with the exception of only one case of d = 10 for variance in the 10 different d-value sets. Therefore, these two parameters (entropy and variance) are suited for discrimination between nevus and MM cells.

From the above orders of the DIF values in Tables VII and IX, it can be concluded that entropy, contrast, and variance are most suited for discrimination between MM and nevus cells in 405-nm excitation. For entropy and contrast, the distance parameter d = 10 gives the highest DIF of 1.879 and 1.847, respectively, and for variance, d = 2 is the best but the difference in DIF is very small. The probabilities of correct identification of nevus cells are 39.49%, 39.21%, and 39.49% for entropy (d = 10), contrast (d = 10), and variance (d = 10), respectively. The probabilities of correct identification of MM cells are 39.49%, 39.21%, and 39.49% for entropy (d = 10), contrast (d = 10), and variance (d = 10), respectively. These values are much better than those obtained by fractal analysis[6-11].

From the above orders of the DIF values in Tables VIII and X, it can be concluded that prominence, variance, and shade are most suited for discrimination between MM and nevus cells in 488-nm excitation. For shade and variance, the distance parameter d = 10 gives the highest DIF of 1.121 and 1.273, respectively, and for prominence, d = 9 is the best but the difference in DIF is very small. The probabilities of correct identification of nevus cells are 38.9%, 33.3%, and 33.6% for prominence (d = 10), shade (d = 10), and variance (d = 10), respectively. The probabilities of correct identification of MM cells are 38.9%, 33.3%, and 33.6% for prominence (d = 10), shade (d = 10), and variance (d = 10), respectively. These values are much better than those obtained by fractal analysis[6-11].

These findings indicate that the GLCM parameter method, especially GLCM-DIF analysis, is a simple and useful method for identification of suitable parameters for differentiation between different stages of cancers and various types of disease that destroy cell structures.

Table VII. Orders of the DIF values among the nine parameters (405-nm excitation).

d	ASM	Contrast	Correlation	Entropy	Homogeneity	IDM	Prominence	Shade	Variance
1	4	8	3	2	6	7	9	5	1

Peer-reviewed version available at Bioengineering 2018, 5, 67; doi:10.3390/bioengineering5030067

2	5	4	3	2	6	7	9	8	1
3	3	6	4	2	5	7	9	8	1
4	3	4	5	2	6	7	9	8	1
5	3	4	7	2	5	6	8	9	1
6	4	3	7	2	5	6	8	9	1
7	4	3	7	2	5	6	8	9	1
8	6	3	7	1	5	4	8	9	2
9	6	3	7	1	5	4	8	9	2
10	4	2	7	1	5	6	8	9	3

Table VIII. Orders of the DIF values among the nine parameters (488-nm excitation).

d	ASM	Contrast	Correlation	Entropy	Homogeneity	IDM	Prominence	Shade	Variance
1	7	4	5	6	8	9	1	3	2
2	7	5	4	6	8	9	1	3	2
3	6	7	5	4	8	9	1	3	2
4	6	9	4	5	8	7	1	3	2
5	5	7	6	4	9	8	1	3	2
6	5	9	6	4	8	7	1	3	2
7	5	9	8	4	7	6	1	3	2
8	5	7	6	4	8	9	1	3	2
9	5	8	9	4	7	6	1	3	2
10	5	6	9	4	7	8	1	3	2

Table IX. Calculated values of DIF for the nine GLCM parameters (average of 4 data).

d	ASM	Contrast	Correlation	Entropy	Homogeneity	IDM	Prominence	Shade	Variance
1	1.274	0.589	1.423	1.504	0.623	0.602	0.2413	0.6622	1.832
2	1.525	1.581	1.659	1.799	1.408	1.369	0.0372	0.4588	1.860
3	1.376	1.059	1.256	1.641	1.065	1.000	0.0783	0.5325	1.844

Peer-reviewed version available at Bioengineering 2018, 5, 67; doi:10.3390/bioengineering5030067

4	1.419	1.225	1.205	1.685	1.169	1.066	0.0692	0.3591	1.835
5	1.452	1.365	1.195	1.708	1.291	1.206	0.1987	0.1744	1.827
6	1.465	1.486	1.212	1.734	1.332	1.240	0.2988	0.0120	1.814
7	1.498	1.604	1.256	1.797	1.430	1.329	0.3670	0.1179	1.802
8	1.524	1.710	1.308	1.820	1.658	1.665	0.4063	0.2081	1.802
9	1.543	1.792	1.347	1.854	1.750	1.789	0.4205	0.2625	1.816
10	1.555	1.847	1.350	1.879	1.512	1.386	0.4054	0.2837	1.836

Table X. Calculated values of DIF for the nine GLCM parameters (average of 48 data).

d	ASM	Contrast	Correlation	Entropy	Homogeneity	IDM	Prominence	Shade	Variance
1	0.334	0.603	0.415	0.372	0.175	0.127	1.374	1.052	1.268
2	0.365	0.474	0.507	0.429	0.049	0.005	1.412	1.063	1.268
3	0.376	0.367	0.428	0.473	0.042	0.015	1.451	1.074	1.269
4	0.407	0.074	0.614	0.528	0.112	0.123	1.452	1.08	1.27
5	0.421	0.11	0.291	0.549	0.082	0.094	1.477	1.084	1.271
6	0.449	0.061	0.336	0.582	0.217	0.228	1.465	1.088	1.272
7	0.456	0.206	0.279	0.606	0.282	0.285	1.453	1.094	1.273
8	0.462	0.327	0.399	0.61	0.26	0.248	1.459	1.102	1.273
9	0.472	0.248	0.084	0.627	0.317	0.325	1.479	1.108	1.273
10	0.473	0.367	0.137	0.628	0.315	0.312	1.472	1.121	1.273

In the above analysis, DIF was calculated using the average of the parameters taken from the four images. To further utilize the parameters obtained by the GLCM analysis, we assessed them by taking the dispersion of the distribution of the parameters into account. The mean and distribution (= dispersion) were fitted with a Gaussian distribution as shown in Figs. 8 and 9 for all nine parameters. The Figures show that the values of the parameters are well distributed and that the values corresponding to the nevus and MM cells are overlapping each other. Using the distribution function, DIF was then calculated and plotted against the parameter values for the distance d = 10. The results are shown in Figs. 10 and 11.

Preprints (www.preprints.org) | NOT PEER-REVIEWED | Posted: 19 June 2018 doi:10.20944/preprints201806.0303.v1

Peer-reviewed version available at Bioengineering 2018, 5, 67; doi:10.3390/bioengineering5030067

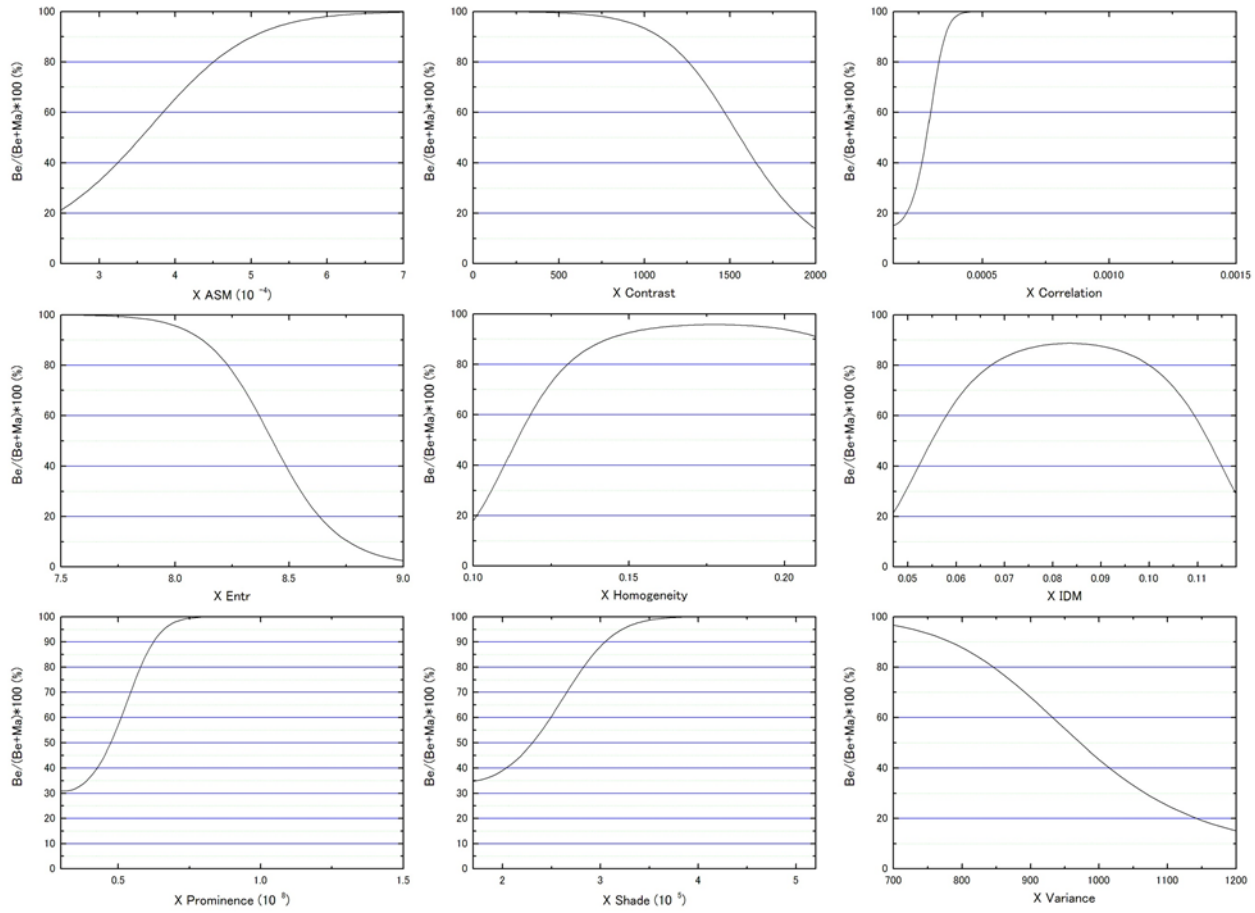

Figure 10. DIF plotted against the parameter values for the distance d = 10 in 405-nm excitation.

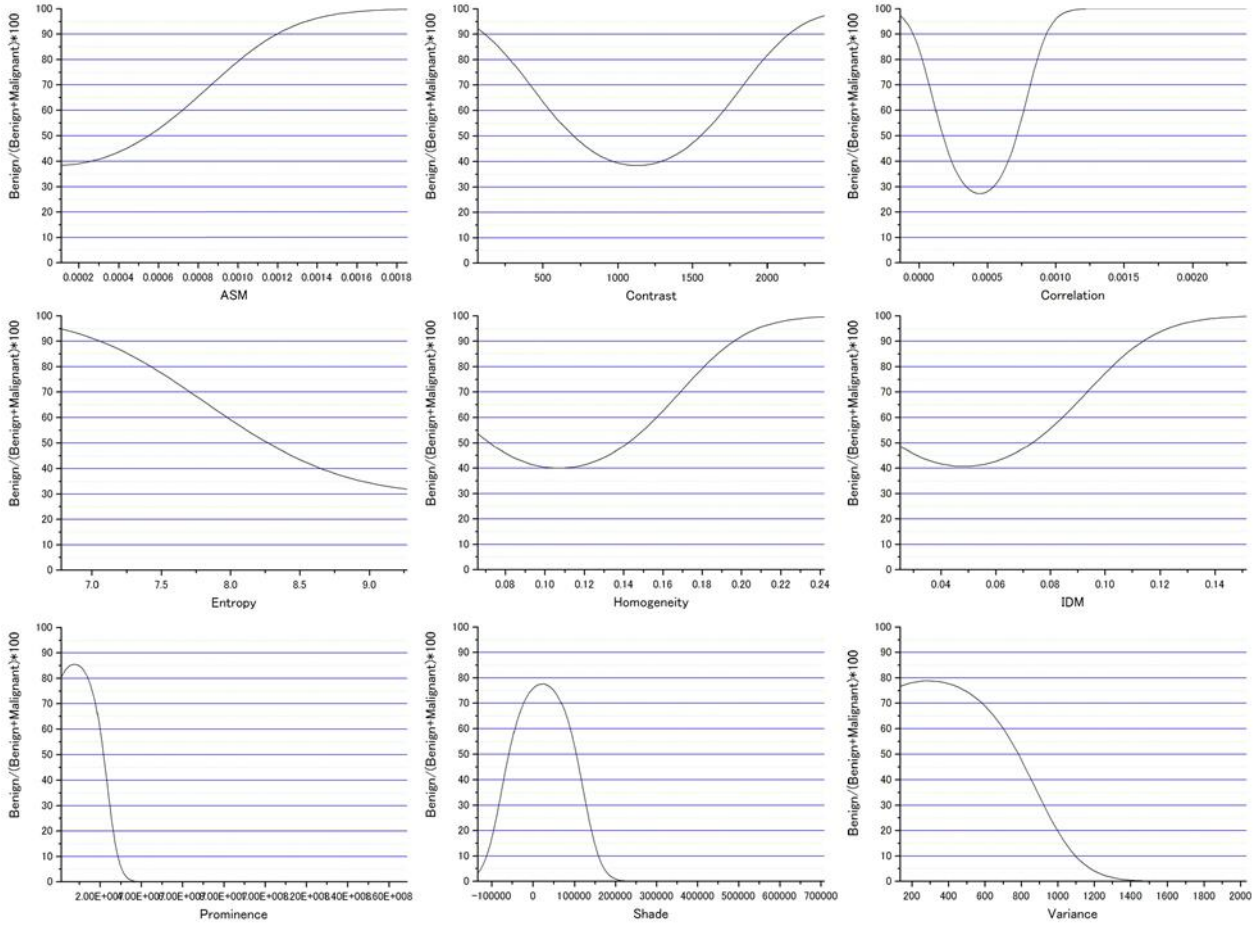

Figure 11. DIF plotted against the parameter values for the distance d = 10 in 488-nm excitation.

We evaluated the appropriateness of assigning either nevus or MM using the discrimination level of the two. For this, we used a "clearness discrimination parameter" (DISC value), which is given by the following equation for each parameter:

DISC = {(65% of DIF value) − (35% of DIF value)} / {(parameter at 65% of DIF value) / 2 + (parameter at 35% of DIF value) / 2} (13)

Here, 35% of the DIF value means that the value of the corresponding parameter has 35% of the maximum intensity for the corresponding parameter. Usually, 90% and 10% are used for the level of discrimination or for steepness evaluation; for some of the parameters, however, the DIF value did not reach 10% for any parameter in the present analysis. The DISC value is used as a criterion of the discrimination between nevus and MM cells. The smaller the DISC value the better discrimination can be performed. For the most effective application of GLMC analysis, we introduced discrimination parameter DISC in the GLCM calculation result on the PT image. In the 405 nm excitation image, DISCs for nevus and MM, Entropy and Homogeneity are small, which is effective for that discrimination. Also, in the GLCM calculation result on the 488 nm excitation image, DISCs for nevus and MM, Entropy and Prominence are small. Thus there are differences in effective parameters due to differences in excitation wavelength. This can be well explained in terms of the sensitivity of the signal intensity to the components in the cells namely melanoma and porphyrin due to the difference in the absorption crossection between them.

Table XI. Value of DISC for the nine GLCM parameters (405-nm excitation).

Parameter	65%	35%	DISC
Entropy	8.34	8.52	0.021
Homogeneity	0.121	0.108	0.112
Variance	913	1040	0.13
IDM	0.0598	0.0508	0.162
Contrast	142	1700	0.182
Correlation	3.04	2.52	0.188
ASM	3.98	3.06	0.264
Prominence	5.25×10^{8}	3.86×10^{8}	0.306
Shade	256900	173000	0.39

Table XII. Value of DISC for the nine GLCM parameters (488-nm excitation).

Parameter	40%	60%	DISC
Entropy	8.64	7.97	0.080

Peer-reviewed version available at Bioengineering 2018, 5, 67; doi:10.3390/bioengineering5030067

Prominence	2.34×10^{7}	1.99×10^{7}	0.159
Correlation	6.47	7.65	0.166
Variance	856	700	0.200
Shade	117000	888	0.274
Homogeneity	0.107	0.157	0.378
IDM	0.0480	0.0842	0.547
Contrast	968	544	0.560
ASM	2.60×10^{-4}	7.20×10^{-4}	0.939

The calculated results are shown in Table XI in ascending order of the DISC value. From this table, it can be concluded that entropy is most useful for discrimination between nevus and MM cells. Homogeneity is also well suited for identification of MM cells in the case of 405 nm pump. This is considered to be due to the change in the density distribution of hemoglobin introduced by the canceration process.

The calculated results are shown in Table XII in ascending order of the DISC value. From this table, it can be concluded that entropy is most useful for discrimination between nevus and MM cells. Prominence is also well suited for identification of MM cells in the case of 488nm pump. This may be induced by the change in the density distribution of melanin introduced by the canceration process. The difference between the calculation results for experiments performed with excitation at 405 and 488 nm can be explained in more detail as follows.

According to the molar extinction coefficients at 405 and 488 nm of melanin in literature http://omlc.ogi.edu/news/jan98/skinoptics.html, they are approximately 2,500 and 1,500 (/mol/cm), respectively. On the other hand, the molar extinction coefficients of hemoglobin at 405 and 488 nm, which is thought to increase uniformly by cellular cancelation, is about 275,000 and 16,000 (/mol/cm), respectively. In both cases, the molar extinction coefficient of hemoglobin is high, but the absolute values are quite different. The extinction coefficient at 488 nm of hemoglobin is 10 times larger than that of melanin, while the coefficient of hemoglobin at 405 nm is 100 times larger than that of melanin. The amount of melanin contained in the cell slice is more than the amount of hemoglobin by much more than 10 times in the sample. Hence, it is considered that the state or degree of canceration of the skin-cell tissue can be monitored with GLCM analysis of 488 nm-pump images.

This can also be inferred from the calculation result. In 488 nm excitation, Prominence and Entropy can be used for benign-malignancy determination, which indicates that morphological change induced by the canceration of cells is captured by the distribution of melanin.

On the other hand, at 405 nm excitation, Homogeneity and Entropy can be used for benign-malignancy discrimination, this may correspond to the morphological change in hemoglobin distribution induced by cellular canceration. This is an indirect method for the discrimination of canceration not using MM. However, it may open a way to utilize a multicolor characterization of component distribution induced by some pathological change in an ensemble of cells.

Furthermore it is of interest find out that in the case of 488nm pump the Prominence increase from nevus cell to malignant, while it is reversed for Homogeneity in 405nm pump condition. This may indicate that canceration induces some kind of chaotic behavior to destroy homogeneity resulting in a “Prominent” characteristic morphological structure.

Peer-reviewed version available at Bioengineering 2018, 5, 67; doi:10.3390/bioengineering5030067

In view of the purpose of this study, it can be concluded that melanin observation by 488 nm excitation is more suitable for determination of canceration, so the conclusion is that Entropy and Prominence at 488 excitation are suitable for benign-malignancy determination. By utilizing 405 nm excitation, we may be able to study the effect of canceration on the hemoglobin-containing tissues such as muscle attached to the sample slices. In this case, Homogeneity and Entropy can be used for benign-malignancy determination, this may correspond to the morphological change in hemoglobin distribution induced by cellular canceration. This means that the spatial distribution of canceration can be investigated through hemoglobin.

5. Conclusions

Label-free confocal photothermal (CPT) microscopy combined with a texture analysis method was utilized for the first time to investigate benign-malignancy determination in mouse skin cells. A Grey Level Cooccurrence Matrix (GLCM) method for texture analysis was applied to the CPT images of malignant melanoma (MM) to study differences in intracellular super-resolved structural properties between MMs and nevus cell. We introduced discrimination parameter DISC in the GLCM calculation result on the PT image. Prominence and Entropy can be used for benign-malignancy determination at 488 nm excitation, which indicates that morphological change induced by the canceration of cells is captured by the distribution of melanin. On the other hand, at 405 nm excitation, Homogeneity and Entropy can be used for benign-malignancy discrimination, this may correspond to the morphological change in hemoglobin distribution induced by cellular canceration. The differences in effective parameters due to differences in excitation wavelength can be well explained in terms of the sensitivity of the signal intensity to the components in the cells namely melanoma and porphyrin (hemoglobin) due to the difference in the absorption crossection between them.

References

1. American Cancer Society, Melanoma skin cancer overview, http://www.cancer.org/acs/groups/cid/documents/webcontent/003063-pdf. 2015; Date of access: 02/09/2015.
2. Siegel, R. L.; Miller, K. D.; Jemal, A. CA Cancer J. Clin. 65, 5-29 (2015).
3. Rigel, D. S.; Carucci, J. A. CA Cancer J. Clin. 50, 215-36 (2000).
4. Soyer, H. P.; Smolle, J.; Kerl, H.; Stetner, H. Lancet 2, 803 (1987).
5. Nachbar, F.; Stolz, W.; Merkle, T.; Cognetta, A. B.; Vogt, T.; Landtthaler, M.; Bilek, P.; BraunFalco, O.; Plewig, G. J. Am. Acad. Dermatol. 30, 551-559 (1994).
6. Ahammer, H.; DeVaney, T. T. J.; Tritthart, H. A. Eur. Biophys. J. 30, 494-499 (2001).
7. Baish J. W.; Jain, R. K. Fractals and cancer. Cancer Res. 60, 3683-3688 (2000).
8. Bedin, V.; Adam, R. L.; de Sa, B. C. S.; Landman, G.; Metze, K. Cancer 10, 260 (2010).
9. Guz, N. V.; Dokukin, M. E.; Woodworth, C. D.; Cardin, A.; Sokolov, I. Nanomed. Nanothechnol. 11, 1667-1675 (2015).
10. Davies, N. A.; Harrison, N. E.; Morris, R. H. K.; Noble, S.; Lawrence, M. J.; D'Silva, L. A.; Broome, L.; Brown, M. R.; Hawkins, K. M.; Williams, P. R.; Davidson, S.; Evans, P. Thromb Haemostasis 114, 1251-1259 (2015).
11. Waliszewski, P.; Wagenlehner, F.; Gattenlöhner, S.; Weidner, W. The Prostate 75, 399-414 (2015).
12. Klein, K.; Maier, T.; Warneken, V. C. H.; Spatz, J. P. Nano Lett. 13, 5474-5479 (2013).
13. Jimbow, K.; Miyake, Y.; Homma, K.; Yasuda, K.; Izumi, Y.; Tsutsumi, A.; Ito, S. Cancer Res. 44, 1128-1134 (1984).
14. Matthews, T. E.; Piletic, I. R.; Selim. M. A.; Simpson, M. J.; Warren, W. S. Sci. Transl. Med. 3, 71ra15 (2011).
15. Zonios, G.; Dimou, A.; Bassukas, I.; Galaris, D.; Tsolakidis, A.; Kaxiras, E. J. Biomed. Opt. 13, 014017 (2008).
16. Tokeshi, M.; Uchida, M.; Hibara, A.; Sawada, T.; Kitamori, T. Anal. Chem, 73, 2112-2116 (2001).
17. Selmke, M.; Braun. M.; Cichos, F. ACS Nano 6, 2741-2749 (2012).
18. Selmke, M.; Cichos, F. Phys. Rev. Lett. 110, 103901 (2013).

19. Boyer, D.; Tamarat, P.; Maali, A.; Lounis, B.; Orrit, M. Science 297, 1160-1163 (2002).
20. He, J.; Miyazaki, J.; Wang, N.; Tsurui, H.; Kobayashi, T. Opt. Lett. 40, 1141-1144 (2015).
21. Lu, S.; Min, W.; Chong, S.; Holtom. G. R.; Xie, X. S. Appl. Phys. Lett. 96, 113701 (2010).
22. Nedosekin, D. A.; Galanzha, E. I.; Dervishi, E.; Biris, A. S.; Zharov. V. P. Small 10, 135-142 (2014).
23. Nedosekin, D. A.; Juratli, M. A.; Sarimollaoglu, M.; Moore, C. L.; Rusch, N. J.; Smeltzer, M. S.; Zharov, V. P.; Galanzha. E. I. J. Biophotonics 6, 523-533 (2013).
24. Moreau, J.; Loriette, V. Opt. Lett. 29, 1488-1490 (2004).
25. Miyazaki, J.; Tsurui, H.; Hayashi-Takagi, A.; Kasai, H.; Kobayashi. T. Opt. Exp. 22, 9024-9032 (2014).
26. Miyazaki, J.; Iida, T.; Tanaka, S.; Hayashi-Takagi. A.; Kasai, H.; Okabe, S.; Kobayashi. T. Biomed. Opt. Exp. 7, 1702 (2016).
27. Miyazaki, J.; Tsurui, H.; Kawasumi, K.; Kobayashi. T. Opt. Lett. 40, 479-482 (2015).
28. Kato, M.; Takeda, K.; Kawamoto, Y.; Tsuzuki, T.; Hossain, K.; Tamakoshi, A.; Kunisada, T.; Kambayashi, Y.; Ogino, K.; Suzuki, H.; Takahashi, M.; Nakashima. I. Cancer Res. 64, 801-806 (2004).
29. Kumasaka, M. Y.; Yajima, I.; Hossain, K.; Iida, M.; Tsuzuki,T.; Ohno, T.; Takahashi, M.; Yanagisawa, M.; Kato, M. Cancer Res. 70, 24-29 (2010).
30. Yajima, I.; Kumasaka, M. Y.; Naito, Y,; Yoshikawa, T.; Takahashi, H.; Funasaka, Y.; Suzuki, T.; Kato, M. Am. J. Cancer Research. 2, 322-329 (2012).
31. Pantic, I.; Pantic, S.; Paunovic, J; Perovic, M. An. Acad. Bras. Ciênc. 85, 1063-1072 (2013).
32. Gebejes, A.; Huertas, R. Texture characterization based on grey-level co-occurrence matrix, 2nd International Conference of Informatics and Management. in Proceedings of the conference of informatics and management sciences. ICTIC 2013; 375–378.
33. Losa, G. A.; Castelli, C. Cell Tissue Res. 322, 257-267 (2005).
34. Honeycutt, C. E.; Plotnick, R. Computers & Geosciences 34, 1461-1472 (2008).
35. Xian, G. Expert Systems with Applications 37, 6737-6741 (2010).
36. Kim, T. Y.; Cho, N. H.; Jeong, G. B.; Bengtsson, F.; Choi, H. K. Computational and Mathematical Methods in Medicine 2014, Article ID 536217: 12 (2014).
37. Pantic, I.; Pantic, S.; Jovanovic, B. Microsc. Microanal. 18, 470-475 (2012).
38. Parker. J. R. Algorithms for image processing and computer vision. John Wiley and Sons 1997; 150-175.
39. Walker, R. F.; Jackway, P.; Longstaff, I. D. Improving Co-occurrence Matrix Feature Discrimination. In DICTA '95, 3rd Conference on Digital Image Computing: Techniques and Application 1995; 643-648.